Cu/Ag Sphere Segment Void Array as Efficient Surface Enhanced Raman Spectroscopy Substrate for Detecting Individual Atmospheric Aerosol

Xu Dong[a,b], Lukas Ohnoutek[c,d], Yang Yang[a], Yiqing Feng[a], Tao Wang[a], Muhammad Ali Tahir[a], Ventsislav K. Valev [c,d], Liwu Zhang[a,b]*

[a] Shanghai Key Laboratory of Atmospheric Particle Pollution and Prevention, Department of Environmental Science & Engineering, Fudan University, Shanghai, 200433, China

[b] Shanghai Institute of Pollution Control and Ecological Security, Shanghai, 200092, China

[c] Centre for Photonics and Photonic Materials, University of Bath, Bath, BA2 7AY, UK

[d] Centre for Nanoscience and Nanotechnology, University of Bath, Bath, BA2 7AY, UK

Corresponding Author

*Liwu Zhang

Email: zhanglw@fudan.edu.cn

ABSTRACT. Surface enhanced Raman spectroscopy (SERS) shows great promise in studying individual atmospheric aerosol. However, the lack of efficient, stable, uniform, large-array and low-cost SERS substrates constitutes a major roadblock. Herein, a new SERS substrate is proposed for detecting individual atmospheric aerosol particles. It is based on sphere segment void (SSV) structure of copper and silver (Cu/Ag) alloy. The

SSV structure is prepared by electrodeposition method and presents a uniform distribution, over large 2 cm^2 arrays and at low cost. The substrate offers a high SERS enhancement factor (due to Ag) combined with lasting stability (due to Cu). The SSV structure of the arrays generates high density of SERS hot spots ($1.3\times10^{14}/cm^2$), making it an excellent substrate for atmospheric aerosol detection. For stimulated sulfate aerosols, the Raman signal is greatly enhanced (>50 times), an order of magnitude more than previously reported substrates for the same purpose. For ambient particles, collected and studied on a heavy haze day, the enhanced Raman signal allows ready observation of morphology and identification of chemical components, such as nitrates, and sulfates. This work provides an efficient strategy for developing SERS substrate for detecting individual atmospheric aerosol.

KEYWORDS: SERS, individual atmospheric aerosol, Cu/Ag SSVs, uniform, low cost

INTRODUCTION

Atmospheric aerosol particles have an important impact on climate by scattering solar radiation and nucleating cloud droplets, which modify the properties of clouds.[1-4] However, the specific organic species formed in the particle phase, particle-to-particle variability, internal structure, phase state (i.e., liquid−liquid phase separations), and particle evolution in the atmosphere remain poorly understood.[5-10] Single particle level analysis is especially important because the particle composition, mixing state, and internal structure determine optical properties and water uptake ability. Methods enabling more detailed and quantitative investigations of aerosol particle properties are necessary in order to improve mechanistic understanding of multiphase aerosol processes occurring in the atmosphere.

Over the past decade, Raman microspectroscopy has emerged as an analytical technique for chemical characterization of aerosol particles.[11, 12] In the field of atmospheric research, Raman spectroscopy successfully probes the properties of airborne particles at ambient temperature and pressure, such as chemical composition,[13] water solubility,[14] pH distribution,[15] reaction and phase transition,[16] efficiency of light

absorption,[17] etc. In comparison to other detection methods, Raman spectroscopy analysis has many advantages, including low cost, non-destructive analysis, minimal sample preparation, visualization, and single particle detection.[18, 19] It can provide detailed information about the presence of functional groups, size, morphology, and the mixing of secondary chemical species with primary components.[20, 21] However, both particle size and concentration of chemical species can limit Raman microspectroscopic studies of aerosol particles. Surface enhanced Raman spectroscopy (SERS) enables the detection of trace organic and/or inorganic species present within particles.[22] Also, it allows the observation of complex inter- and intraparticle variability, as well as the characterization of smaller aerosol particles, whose diameter (<150 nm and well below the diffraction limit) makes them more atmospherically-relevant.[23] In comparison to traditional vibrational spectroscopy techniques, SERS offers much better potential for characterization of the physicochemical properties of aerosol particles. Meanwhile, a few variations of SERS, such as tip-enhanced Raman spectroscopy (TERS),[24] electrospray SERS (ES-SERS),[13, 25] and surface-enhanced resonance Raman spectroscopy (SERRS) of trapped and suspended particles,[26] have also been applied to study aerosol particles.

Following preliminary, qualitative studies that illustrated SERS' potential for probing bioaerosols,[27-29] the technique has recently been applied to aerosol particles more broadly and in a more quantitative manner. In 2015, Craig et al.[30] used silver nanoparticle coated quartz substrates to investigate both ammonium sulfate and sodium nitrate aerosol particle standards, as well as ambient aerosol. In 2016, Fu et al.[31] used Klarite, a commercial Au substrate of structured gold inverted pyramids, to study ammonium sulfate and naphthalene mixed particles. In 2018, Tirella et al.[23] used Ag foil as SERS substrate to study atmospheric aerosol particles and improved the limit of detection in terms of particles size to 400 nm. Sun et al.[32] also used Ag foil as SERS substrate to directly observe the sulfate–nitrate–ammonium components in atmospheric single particles. The reported enhancement factors (EFs) ranged from 2.0 to 70 for $\nu_s(SO_4^{2-})$, $\nu_s(NO_3^-)$, ν(C-H), ν(O-H), and δ(C-C) vibrational modes[13, 30-32] and rose to 10^5 for vibrational modes of Rhodamine 590 chloride (R6G), a dye with a large

scattering cross-section commonly used for SERS studies.[26] However, there are several shortcomings of using substrates such as Ag nanoparticle-coated quartz, Ag foil or Klarite. For example, it is expensive to make Klarite substrate, which is no longer available, for commercial reasons. In the case of Ag nanoparticle substrates, low measurement reproducibility and low enhancement factors due to the lack of uniformity in the distribution of "hotspots" have hindered wider use of the substrates. By contrast, sphere segment void (SSV) SERS substrates based on nanostructures consisting of hexagonal close-packed arrays of uniform sphere segment cavities exhibit large and reproducible enhancements.[33, 34] These substrates support a variety of plasmon modes and can be fully characterized by white light dispersion measurements allowing the direct identification of the modes predicted by computational models of the nanoscale optical fields.[35] To the best of our knowledge, SSV substrates have never been used for detecting ambient aerosol particles.

In this study, monolayer-ordered copper and silver SSV arrays (Cu/Ag SSVs) SERS substrates were prepared and used for testing the species commonly observed in atmospheric aerosols for the first time. These substrates can be grown uniformly, over a large area at low cost. They offer precise control over the electromagnetic hotspots, which translates into high enhancement factors for SERS. The EFs are shown to be stable and reproducible. To demonstrate real-life applicability of the substrates, both laboratory-generated and ambient aerosol particles were analyzed with SERS, revealing chemical composition and particle size dependences. The reported results highlight the potential for our SSV-mediated SERS analysis of aerosol particles to improve the understanding of physicochemical properties of atmospheric aerosols.

EXPERIMENTAL

Materials. Polystyrene (PS) microspheres (diameter 1.0 μm, 5% w/v) were purchased from Aladdin®. Ethanol, sodium dodecyl sulfate (SDS), copper(Ⅱ) sulfate pentahydrate ($CuSO_4 \cdot 5H_2O$, ≥99.0%), silver sulfate (Ag_2SO_4, ≥99.7%), ammonium sulfate ($(NH_4)_2SO_4$, ≥99.0%), sodium sulfate (Na_2SO_4, ≥99.0%), sodium nitrate

($NaNO_3$, ≥99.0%) and tetrahydrofuran (THF, ≥40.0%) were purchased from Sinopharm Chemical Reagent Co., Ltd. 3, 5-diamino-1, 2, 4-triazole (DAT, 98%) was obtained from Shanghai Wokai Chemical Reagent Co., Ltd. All chemicals were used as received unless further mentioned. Deionized water was used in all experiments.

Self-assembly of 2D Colloidal Monolayer Array of PS Particles. The PS microspheres were sufficiently dispersed in ethanol/water (V/V 1:1) solution by ultrasonic dispersion at a concentration of 5 wt %. A sodium dodecyl sulfate solution (1%, 20 μL) was added to water in a tank with a diameter of 12 cm. Then, the PS microsphere solution was dropped on a flat silica wafer placed, in tilted, at the edge of the tank, and the PS microspheres slipped into the surface of water. Finally, the PS microsphere monolayer was lifted onto the fluorine tin oxide (FTO) coated glass slides. A close packed PS microsphere array was obtained. These slides with microsphere arrays were dried in air.

Electrodeposition of Cu/Ag NPs. The electrodeposition was performed on a CHI 660A electrochemical workstation (CH Instruments Co.). We used a conventional three-electrode cell at room temperature. A 2D PS coated FTO substrate, a Pt foil, and a saturated calomel electrode (SCE) were employed as working, counter, and reference electrodes, respectively. In a typical electrodeposition, 100 mL of aqueous solution containing 0.1 M $CuSO_4 \cdot 5H_2O$ + 10 mM 3, 5-diamino-1, 2, 4-triazole (DAT), with 0.05 M Ag_2SO_4 at pH = 1.5 adjusted by using H_2SO_4, was used as electrolyte. We adopted a two-step multipotential method. At first, the nucleation step, Cu/Ag seeds were obtained under −0.200 V in 20 ms; this process was repeated four times to get a higher seed density. Second, the growth step, Cu/Ag NPs grew under −0.200 V for another 300 s. The as-synthesized Cu/Ag NPs coated FTO coating a 2D monolayer of PS was then cleaned with double-distilled water several times and dried in a stream of high-purity N_2.

Preparation of Cu/Ag SSVs. The as-fabricated Cu/Ag NPs coated FTO coating a 2D monolayer of PS arrays were used to prepare Cu/Ag SSVs. The PS particles were removed by hydrofluoric acid, producing a monolayer-ordered Cu/Ag SSVs arrays

deposited on the FTO substrate. The nanobowl structure was affirmed using Scanning Electron Microscope (SEM; Nova nano SEM 450; FEI, Amercian). The element distribution was shown using Energy Dispersive Spectrometer (EDS; Inca X-max50; Oxford, England).

Sample Collection. 0.1 M solution of ammonium sulfate was used for the laboratory-generated aerosol samples. First, the air flows out of a compressor and into a two-level air filter system (0.1 and 0.01 μm, respectively) to partially remove impurities. Then, the air continues into a two-level air dryer system that can remove nearly 90% percent of the moisture. This is followed by an air filter (0.01 μm) set to prevent the nebulizer from being contaminated by the remaining impurities. The nebulizer generates aerosol droplets with an aerodynamic diameter of 0.5−20 μm, whose median mass aerodynamic diameter range from 1 to 4 μm. Finally, the aerosol droplets are deposited onto substrates using a microanalysis particle sampler. All the samples were collected for 1 min using a homemade microanalysis impactor, operating at a flow rate of 5 lpm. The microanalysis impactor consisted of a mini pump, a flow meter, and a sampling head. Then we accelerated the dehydration by increasing the temperature to 50 °C. The real atmospheric aerosol particles were collected on the roof of the environmental science building at Fudan University in the afternoon of November 28th, 2018. The weather was cloudy with a northeast breeze, and the real-time PM 2.5 index was 158 (data were provided by Shanghai Meteorological Bureau). The samples were collected for 12 h using Anderson 8 grading particle sampler (NVA-800; Staplex, USA).

Raman Spectroscopy Measurement. The Cu/Ag SSVs substrates and the aerosol particles were probed by using an XploRA Plus confocal spectrometer (Jobin Yvon, Horiba Gr, France). The Raman spectra measurements were recorded using the 532 nm laser excitation and a 100× Olympus microscope objective lens. The confocal slit width was 100 μm, and exposure time was 5 s and number of accumulations were 10, detecting a spectral region of 100 to 2000 cm^{-1}. When Raman mapping was acquired, the exposure time was 2 s and number of accumulations were chosen to be 10. The mapping area was 50 × 50 μm^2 with a step size of 2 μm.

FDTD Simulation. Lumerical FDTD[36] (finite-difference time-domain) software was used to perform numerical simulation of electromagnetic fields near the surface of the SSVs with varying dimensions. FDTD is a method for numerically solving Maxwell's equations.[37-39] A mesh is created in the simulated region, a light pulse introduced and its propagation calculated in the time-domain using the optical constants of the media in the simulated region. The main source of error comes from calculating the electromagnetic fields for discrete coordinates only. Convergence testing was used to check the validity of the results.

The simulations presented in this work were done for SSVs in a Cu-Ag alloy (1:1). The optical constants of the alloy were approximated using Bruggeman effective medium approximation. For the simulation, the SSVs were arranged in a hexagonal array and periodic boundary conditions were applied at the edges of the unit cell of the array along the x- and y- directions. Perfectly matched layer (PML) boundary conditions[40] were used on the edges of the simulated region perpendicular to the z-axis. A plane wave polarized in the x-direction was incident on the arrays and the electromagnetic fields near the surface were monitored. The color maps presented here show $|E|/|E_{incident}|$, where $|E|$ is the modulus of the calculated electric field and $|E_{incident}|$ is the modulus of the incident electric field, for λ=532 nm which is the wavelength of the laser used in the Raman measurements.

RESULTS AND DISCUSSION

Preparation of Cu/Ag SSVs. Bimetallic Cu/Ag SSVs with various Cu and Ag proportions were prepared by electrodeposition method with polystyrene (PS) monolayer film as template. The scanning electron microscopy (SEM) images of the obtained PS monolayer template and of the Cu/Ag SSVs are shown in Figure 1 (a) and (b), respectively. Figure 1 (a) demonstrates excellent short-range order with only minor size defects. Figure 1 (b) demonstrates good long-range order in the Cu/Ag SSVs, prepared using the electrodeposition method. An enlarged view of Figure 1 (b) is presented in Figure 1 (c), showing well-defined bowl structures.

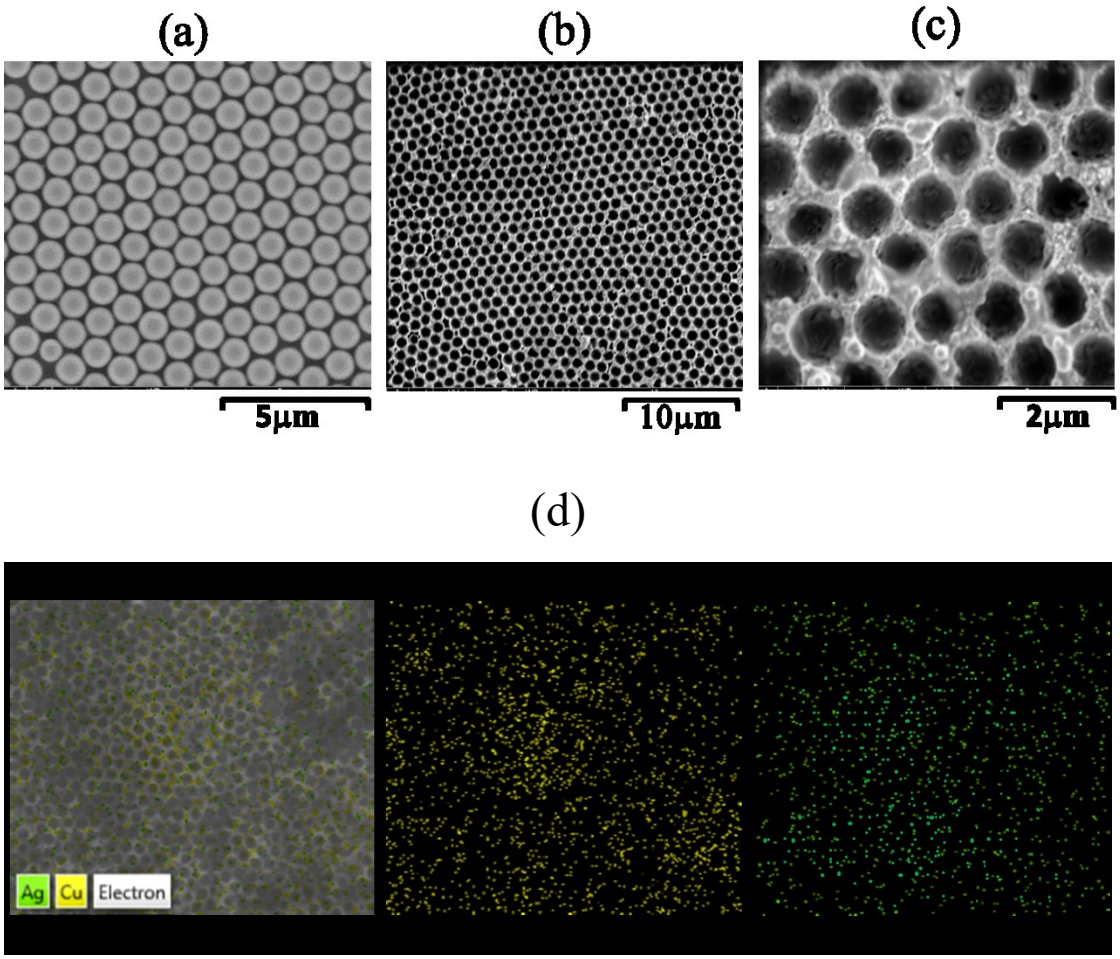

Figure 1. Geometrical structure and element composition of the samples. In (a), a scanning electron microscopy (SEM) image of polystyrene (PS) monolayer film demonstrates excellent short range order. In (b), SEM of Cu/Ag sphere segment voids (SSVs) shows good long-range order (molar ratio n_{Cu}:n_{Ag}=1:1). In (c), enlarged view of the SEM from Cu/Ag SSVs reveals an overall well-defined geometry of the array. In (d), element energy dispersive spectroscopy (EDS) mapping of the Cu/Ag SSVs (molar ratio n_{Cu}:n_{Ag}=1:1).

For enhancing Raman signals, Ag is considered superior to other noble metals, such as Au and Cu.[41] The reason is that Ag exhibits stronger surface electric field under plasmonic resonant excitation condition than Au and Cu.[42] However, in the case of Ag, ambient SERS performance decreases because the oxidized Ag surface hinders the

charge transfer to the analyte molecule, which is part of the chemical signature enhancement mechanism.[43] In addition, the preparation of Ag nanobowls with uniform shape and narrow size distribution has proven challenging,[44] and Ag nanobowls are rather instable and change spontaneously into microspheres in aqueous solutions.[45] An effective approach to stabilize Ag is to produce Cu/Ag bimetallic structures. For copper and sliver nanoalloy, the Ag nanoparticles initially wetting the Cu nanoparticle along its {111} surfaces at one or multiple locations forming epitaxial Ag/Cu (111) interfaces, followed by Ag atoms diffusing along the Cu surface. Then stable nanobowl structure can be formed.[46] Adding Cu to Ag and varying the molar ratio of Cu to Ag does not compromise the geometry of the SSVs. Figure 1 (d) shows an Element Energy Dispersive Spectroscopy (EDS) mapping of the SSVs, at 1:1 Cu/Ag dosage, where the signals of Cu and Ag elements are clearly observable. In the EDS images of the Cu/Ag SSVs, the element distribution of Ag and Cu is uniform, indicating that Ag^{+} and Cu^{2+} was deposited at the same time.

The electromagnetic properties of the Cu/Ag SSVs can be tuned by varying the diameter of the voids. To demonstrate control over the void diameter, a series of Cu/Ag SSVs were synthesized by changing the time of electrochemical deposition, keeping constant the used amounts of Cu and Ag in the reaction system. The Raman optical micrograph in Figure S1 demonstrates that the PS monolayer is highly ordered. After etching with tetrahydrofuran (THF), their, are shown in Figure S2. The highly ordered grid structure of the obtained Cu/Ag SSVs can be clearly observed. Their average void diameter and wall thickness (including statistical variations) were obtained from the corresponding SEM images, as shown in Figure 2. The depth of the SSVs were calculated according to the following Eqns (1) or (2).

$$\text{depth} = \frac{d}{2} - \sqrt{\frac{d}{2} - \frac{void\ \ diameter}{2}} \quad \text{(For depth<0.5d)} \qquad (1)$$

$$\text{depth} = \frac{d}{2} + \sqrt{\frac{d}{2} - \frac{void\ \ diameter}{2}} \quad \text{(For depth>0.5d)} \qquad (2)$$

where *d* is the diameter of the sphere used as template.

From 100 s to 300 s, as the electroplating time is prolonged, the average void diameter of Cu/Ag SSVs is elevated, indicating that the SSV structures form gradually.

Meanwhile, the wall thickness of the Cu/Ag SSVs is reduced, until the bowl forms into 1/2 sphere. From 500 s to 900 s, both the void diameter and wall thickness have opposite variation tendency. These results reveal that, when changing the time of electrochemical deposition, the size of the Cu/Ag SSVs can be controlled. In turn, the electromagnetic properties of the SSVs are greatly affected.

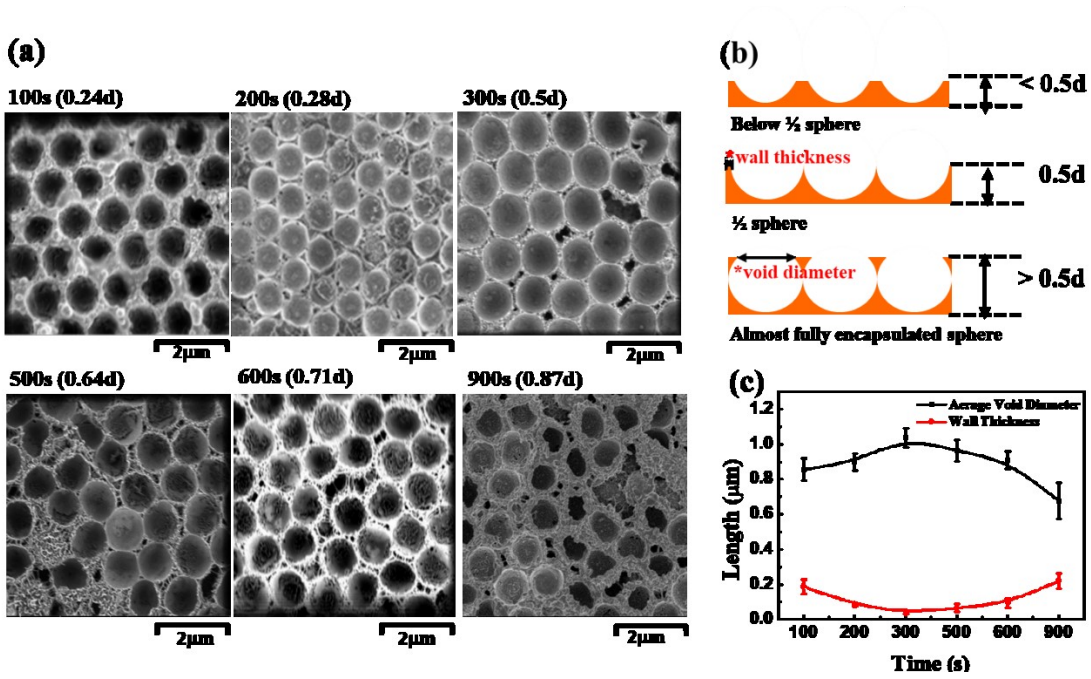

Figure 2. Controlling the diameter of the SSVs by the duration of electroplating. In (a), SEM images of Cu/Ag SSVs with different electroplating time (d: the diameter of the sphere. 0.24d, 0.28d, 0.5d, 0.64d, 0.71d and 0.87d are the depth of the SSVs). In (b), Schematic geometry. In (c), the variation tendency of their average void diameter and wall thickness with different electroplating time (error bar: the relative standard deviations of 50 particles on their SEM images).

FDTD Simulation of Cu/Ag SSVs. To demonstrate the effect of the geometry of SSVs on the local electric field distribution, we conducted numerical simulations using the finite-difference time-domain (FDTD) method. Figure 3 shows the electric field distribution on the longitudinal and transversal sections with respect to the polarization of the incident light for Cu/Ag SSVs with different void diameters. The results shown are for λ=532 nm. In the longitudinal sections (Figure 3 (a)), due to the local charge build up at the edges of the bowl, the electric field hotspots are localized near the sides

and bottom, which strongly couples to the localized surface plasmonic resonance of the Cu/Ag SSVs. Strong field enhancement is observed near the bottom of the cavity, as shown in Figure 3 (a). The intensity of these hotspots is notably increased as the depth of the Cu/Ag SSVs increases at first (corresponding electroplating time from 100 s to 300 s) but then starts to decrease. The strongest electric field near the bottom of the SSV is achieved for the depth equal to the radius of the cavity, with a maximum intensity of about 4 times that of the incident light. The hotspots at the sides slightly shift as the void diameter changes. This is because the void mode and rim contributions have field components aligned in antiphase; in this case, the void field component is forced deeper into the void, as shown in Figure 3 (a) (0.87d) (d: the diameter of the sphere).[35, 47] These results imply that the plasmonic property of Cu/Ag SSVs can be tuned by their bowl depth, which is useful for designing SERS substrates for aerosol particle characterization. In addition, the intense fields located directly at the metal rim are also strongly coupled to incident light and provide efficient excitation of molecules at the surface for SERS.[35] In the transversal sections of Figure 3 (b), the calculated field distributions are in agreement with the results in Figure 3 (a). The plasmonically induced hotspots shift from the surface of the bowl to the inside of the bowl, as the electroplating time prolongs from 100 s to 900 s. The deepest nanobowl has large electric field in the middle of the cavity rather than near the surface of the metal. The results indicate that the local field strengths achieved in the simulated SSVs should be sufficient to lead to SERS on resonance with the 532 nm lasers.

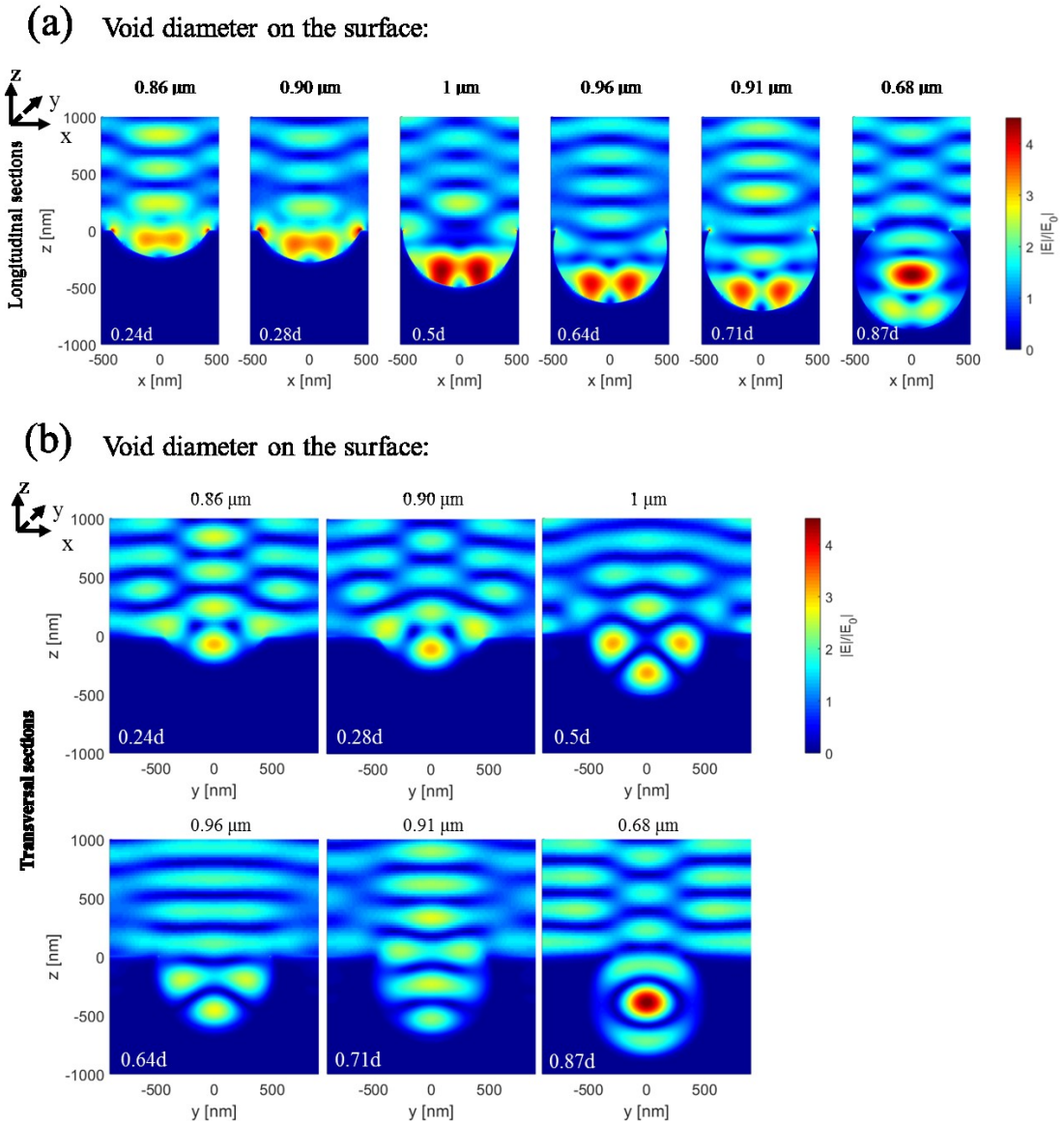

Figure 3. Controlling electromagnetic hotspots with the void diameter. Local electric field distribution for Cu/Ag sphere segment voids (SSVs) irradiated with an x-polarized plane wave of wavelength 532 nm calculated using Lumerical FDTD. (a) The color maps show the electric field distribution in a longitudinal section (with respect to the polarization of the incident light) through the middle of the cavity. The void diameter on the surface changes from left to right. (b) The color maps illustrate the calculated electric field distribution in a transversal section through the centre of the cavity for the same structures as in (a). Areas with enhanced electric field compared to the electric field of the incident light E_0 (hotspots) can be seen for all of

the simulated structures. The electric field strength and the position of the hotspot is strongly dependent on the geometry.

SERS Performance Detection of Cu/Ag SSVs. To demonstrate the performance of Cu/Ag SSVs as SERS substrates, we directly collected $(NH_4)_2SO_4$ aerosols (typical component in atmospheric aerosol) on fluorine tin oxide (FTO) coated glass and on a Cu/Ag SSVs substrate. The SERS spectra of $(NH_4)_2SO_4$ aerosols using FTO or Cu/Ag SSVs (with different molar ratio of Cu and Ag) are shown in Figure 4 (a-1). All spectra have been smoothed by Savitzki–Golay method, and their baselines were corrected for elimination of the fluorescence background between 100 and 2000 cm^{-1} by a polynomial function of the seventh order. The SERS spectra of $(NH_4)_2SO_4$ are characterized by the peaks at 440, 520, 970 and 1100 cm^{-1}. 440 and 970 cm^{-1} are assigned to SO_4^{2-} stretching and 520 and 1100 cm^{-1} are assigned to NH_4^+ stretching, which are in agreement with previously reported data.[48-50] Craig et al.[30] used silver nanoparticle coated quartz as SERS substrate for atmospheric aerosol detection, the average enhancement factor for sulfate was 2. Fu et al.[31] used Klarite as SERS substrate, its average EF for sulfate is 6.1. In this work, for stimulated sulfate aerosols, the Raman signal is greatly enhanced (EF=55 times), an order of magnitude more than previously reported substrates for the same purpose. As the proportion of Ag content is increased, the SERS intensity of $(NH_4)_2SO_4$ aerosols also increases (Figure 4 (a-2)). This effect can be attributed to greater enhancement of the electromagnetic (EM) field associated with strong, localized surface plasmon resonances in Ag. Generally, the values of the enhancement factor are the highest on Ag and relatively very low on Cu, because of an increased surface plasmon resonance, which mainly depends on the permittivity of the corresponding metals. However, the permittivity of a given metal alloy is much more complex and was shown to be strongly affected by the nature of its stoichiometric constituents.[51] Meanwhile, the obtained SERS spectra of Cu/Ag SSVs with different electroplating time are shown in Figure 4 (b-1). In Figure 4 (b-2), with increasing electroplating time, we can distinguish two regimes of increasing SERS intensity: a fast one (below 300 s) and a slow one (above 300 s). These trends can be explained by two

simultaneous effects that result from the increase of electroplating time, on the SERS intensity. On the one hand, within each void, the total surface area increases linearly (following the formula for the area of a spherical cap $A = 2\pi rh$, with r the radius of the void and h the height of the cut-off plane), which leads to linearly increasing SERS intensity. On the other hand, Figure 2 indicates that 300 s corresponds to the largest void diameter of the SSVs, for which Figure 3 demonstrates the highest intensity of surface electromagnetic hotspots. Consequently, the SERS intensity from localized electromagnetic hotspots peaks at 300 s and decreases subsequently. The combined effects of electromagnetic peak at 300 s and linear increase from total surface area is consistent with the observed behavior in Figure 4 (b-2). To test the limits of detection (LOD) of Cu/Ag SSVs substrate, 1 M $(NH_4)_2SO_4$ aerosols were collected on Cu/Ag SSVs made from 1:1 Cu-Ag alloy and 300 s electroplating time. For comparison, samples were collected accordingly on FTO, which served as a non-enhancing substrate. The spectra are shown in Figure S3. It is obvious from the spectra that LOD can be reduced by 10^2 by using Cu/Ag SSVs as SERS substrate.

The Cu/Ag SSVs have several characteristics that are clearly advantageous for improving SERS signals. Firstly, the SSV geometry – bowl-shaped – serves as a light harvester by focusing the light in the cavity. Moreover, the structure could benefit from electromagnetically coupling edge modes with the cavity modes.[52] Secondly, in comparison to a flat substrate surface, the curvature cavity of the Cu/Ag substrate creates well-defined electromagnetic hotspots. Finally, a higher density of SERS hot spots can be generated in the cavity structure arrays compared to that of particles dispersed on a flat surface under the same horizontal projected areas.

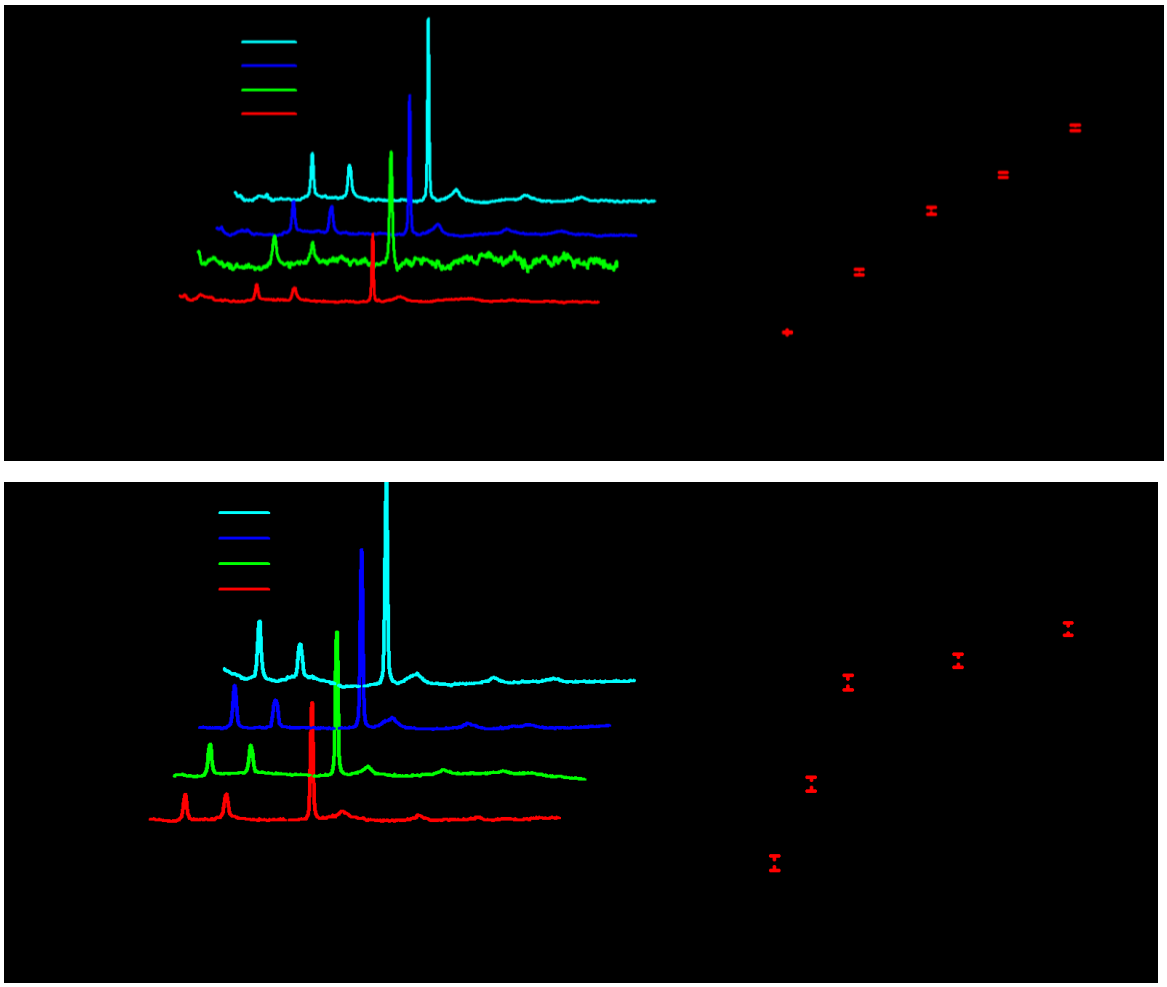

Figure 4. Tuning substrate stability and SERS enhancement factor. SERS spectra of $(NH_4)_2SO_4$ aerosols using FTO or Cu/Ag SSVs with different molar ratio of Cu and Ag as substrate (a-1) and the tendency of intensity at 970 cm^{-1} (a-2); SERS spectra of Cu/Ag SSVs with different electroplating time (b-1) and SERS intensity at 970 cm^{-1} as a function of electroplating time (b-2).

The diameter of the voids, which has an effect on the magnitude of the surface enhancement,[35, 53, 54] was further studied. For efficient surface enhancement, it is necessary to ensure coupling of both the incoming laser light and the outgoing Raman scattered light to plasmon modes of the surface.[55] Template spheres from 500 nm to 2 μm diameter were used for SSV fabrication. Figure 5 (a) shows spectra of $(NH_4)_2SO_4$ aerosols on Cu/Ag SSV substrates with different sphere diameter. It can be seen that, even though the 1 μm sphere structures do not give the highest global intensity, the difference between the background and the peak height, and the signal to noise ratio, is

highest for this sphere diameter. The 500 nm spheres are more difficult to pack uniformly and result in less reproducible SSV substrates. For the 2 μm spheres, the SSV structures show a large background. In this study, 1 μm diameter template spheres were found to give the best signal to background ratio when 532 nm laser is used.

In addition, the effect of $(NH_4)_2SO_4$ particle size on the enhancement factor was studied as well. The size of the $(NH_4)_2SO_4$ aerosols particles selected for study range from 500 nm to 10 μm (Figure S4). Five $(NH_4)_2SO_4$ aerosols particles of different size were selected under Raman Optical Microscope on SSV and FTO, respectively. It is shown in Figure (5b) that the SSV (1μm sphere, n_{Cu}:n_{Ag}=1:1, 0.5d) show comparable enhancement factor for simulated particles with different size. The enhancement factor is only slight lower for particles with large size. This results suggest that the substrate is suitable for aerosol particles with different size.

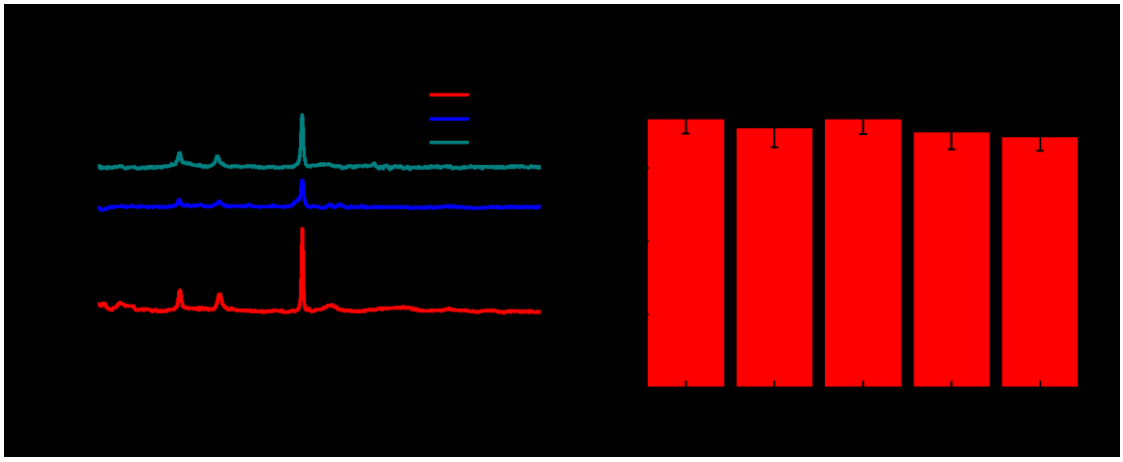

Figure 5. Effects on the enhancement factor of Cu/Ag SSV substrates. Raman spectra of aerosols on Cu/Ag SSV substrates made from different template sphere diameters (a); Enhancement factor for $(NH_4)_2SO_4$ aerosols particles with different size of on the same Cu/Ag SSV substrate (b).

The Cu/Ag SSV substrates' SERS performance is stable over time and highly reproducible. To demonstrate reproducibility, ten SERS measurements were carried out using identical Cu/Ag SSVs as the substrate and the same $(NH_4)_2SO_4$ aerosols as analyte. The Cu/Ag SSVs of Cu-Ag alloy (1:1) and electroplating time (300 s) was used for reproducibility study. Figure 6 (a) shows the SERS spectra of these measurements,

and the relative standard deviation (RSD) of the intensities of their 970 cm^{-1} peaks is 8.8%. The results are clearly reproducible. To demonstrate stability over time, the same Cu/Ag SSVs substrate was used to measure $(NH_4)_2SO_4$ aerosol signals, after a varying substrate storage time – from one week to five weeks – and the results are provided in Figure 6 (b). With the increase of storage time, there is slowly decreased tendency of its SERS intensity at 970 cm^{-1}. This is because the oxidation on the surface of Cu/Ag SSVs. However, even after five weeks, the Raman signal of $(NH_4)_2SO_4$ aerosols present only little change (< 8%). This result shows that the SERS signal based on Cu/Ag SSVs as substrate is highly stable. The high SERS signal reproducibility should arise from the ordered size and shape distribution of Cu/Ag SSVs as substrate.

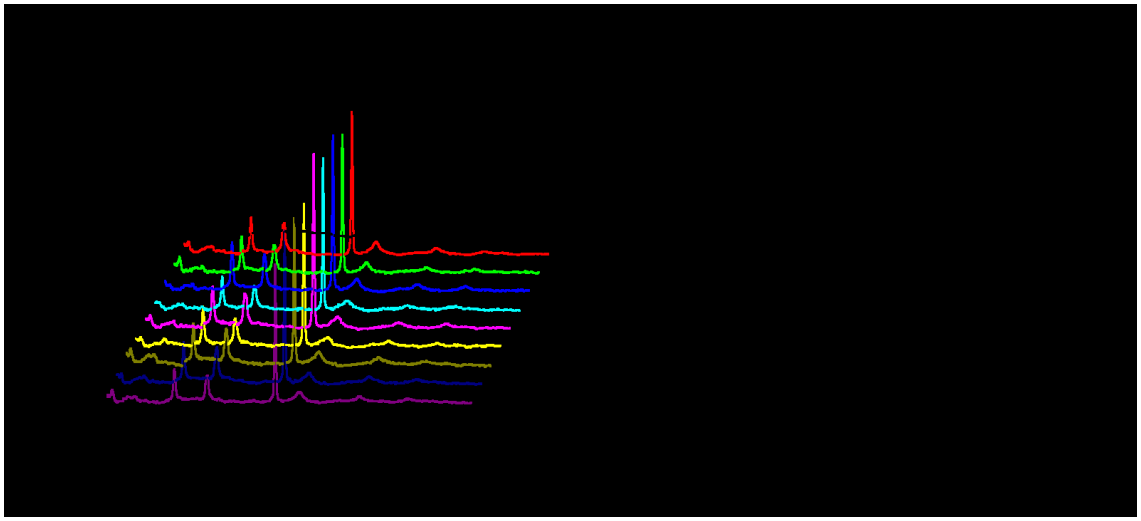

Figure 6. Substrate performance is highly reproducible and stable. Ten SERS measurements using identical Cu/Ag SSVs as the substrate and the same $(NH_4)_2SO_4$ aerosols as analyte (a); The tendency of SERS signals intensity at 970 cm^{-1} with different storage time of Cu/Ag SSVs from one week to five weeks (b)

SERS Detection of Atmospheric Aerosols. The synthesized Cu/Ag SSVs are also effective SERS substrates to probe real-life, atmospheric aerosols. To illustrate this point, we sampled such aerosols on the roof of the environmental science building at Fudan University (global coordinates: 121 °51′ E, 31 °33′ N) in the afternoon of November 28th, 2018. The weather was cloudy with a northeast breeze, and the real-

time PM 2.5 index was 158 (data were provided by Shanghai Meteorological Bureau). For reference, first, we studied the SERS spectra of a mixture of Na_2SO_4 and $NaNO_3$ aerosols that were prepared in laboratory conditions, see Figure 7 (a). Figure 7 (a) shows the characteristic peaks of SO_4^{2-} (454, 621, 985 and 1061 cm^{-1})[49] and NO_3^- (717 and 1051 cm^{-1}).[56] Subsequently, we performed a point-by-point SERS mapping of the atmospheric aerosols, in an area measuring about 2 × 2 μm^2, of the Cu/Ag SSVs substrates, see Figure 7 (b) and (c). As can be concluded from Figure 7 (b) and (c), the real-life atmospheric aerosols are composed of both, nitrate (red) as well as with sulfate (green) components with variable composition.

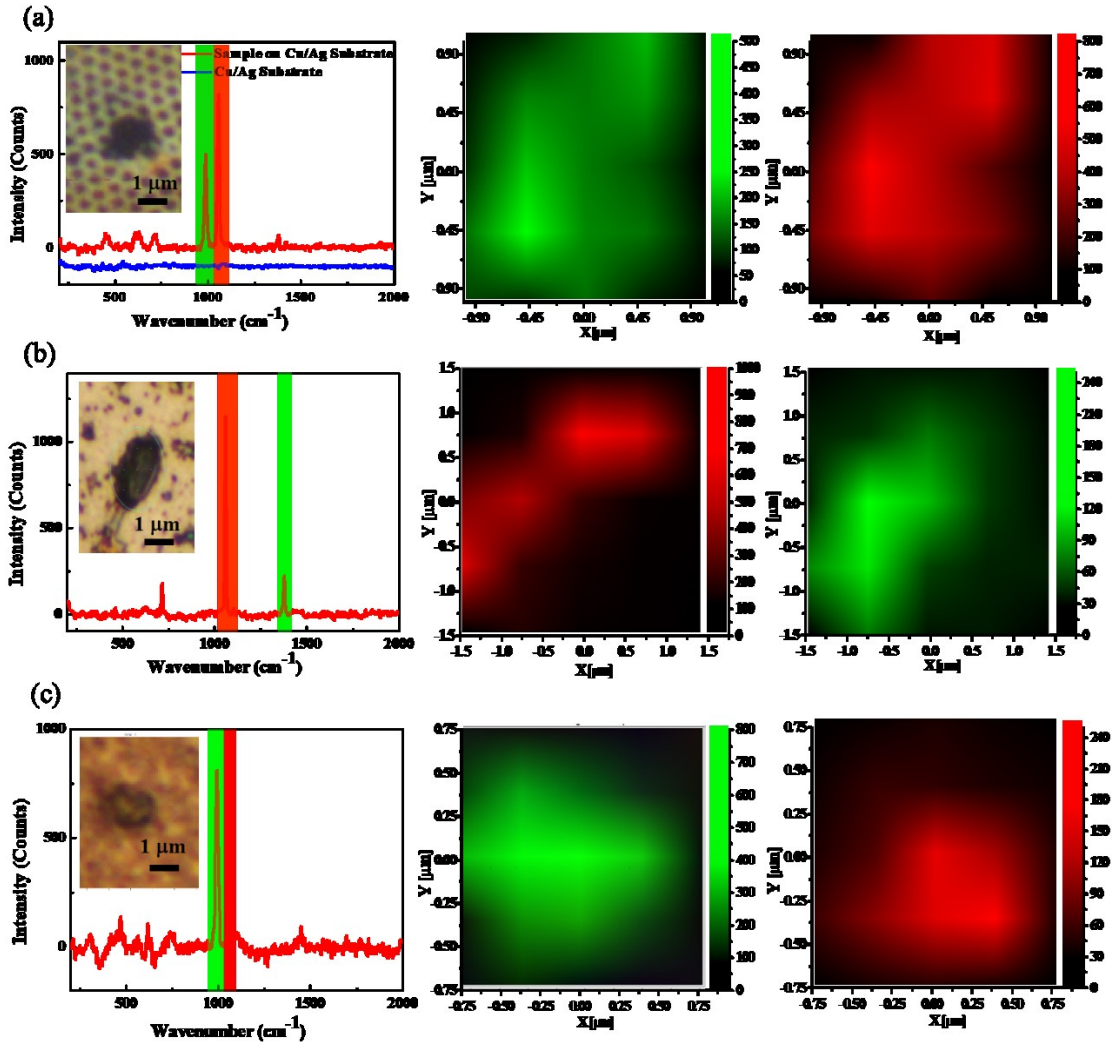

Figure 7. Identifying chemical composition of ambient particles. In (a), SERS spectra and point-by-point Raman mapping of Na_2SO_4 and $NaNO_3$ mixture aerosols prepared in the laboratory are shown, for reference. In (b) and in (c), SERS spectra

and point-by-point Raman mapping of a 2 μm and a 1 μm atmospheric aerosols particles, respectively, are shown. The mapping region is about 10 × 10 μm^2 on the Cu/Ag SSVs substrates.

To further illustrate the environmental application of this SSV substrate, SERS spectra and mapping of the ambient particles were shown in Figure 8. 5 typical ambient particles were chosen and their SERS spectra were shown in Figure 8 (a) and 8 (b). Figure 8 (c) and (d) show the Raman mapping of atmospheric aerosol particles in an area measuring about 50 × 50 μm^2. By mapping, from the contrast of the color, we can directly get the composition information visually. For particles 1, 2 and 4, they have strong nitrates signal, the sulfates signal are very weak or almost cannot be observed (Figure 8 (b)). For particle 3 and 5, they only show sulfates signal. However, in Figure 8 (d) we can observe sulfate signals on the other smaller particles, while nitrate signal is not observed in Figure 8 (c). This may suggest that for atmospheric aerosols of large size on the substrate (around 2 μm), the principal components of the atmospheric aerosols are mostly nitrate (red), with fewer sulfate (green) (Figure 8 (c)). But for 1 μm size of atmospheric aerosols or smaller, most are sulfate (green) and few are nitrate (red (Figure 8 (d)). This phenomenon indicates that the spectra, which can be observed within individual particles on micron spatial scales with SERS is complex and variable. And this data highlights the potential for mapping atmospheric particles with < 1 μm resolution. The results show the potential for SERS to enable improved analysis of aerosol particle chemical composition and mixing state for the different size aerosol particles. The ability to detect chemical species in these small volume particles also shows the potential for future SERS work to probe differences in composition at aerosol surfaces due to phase separation, the presence of surfactants, or surface level reactions. Overall, future SERS studies of atmospheric aerosol composition could lead to improved understanding of multiphase atmospheric processing and aerosol impacts on climate and human health.

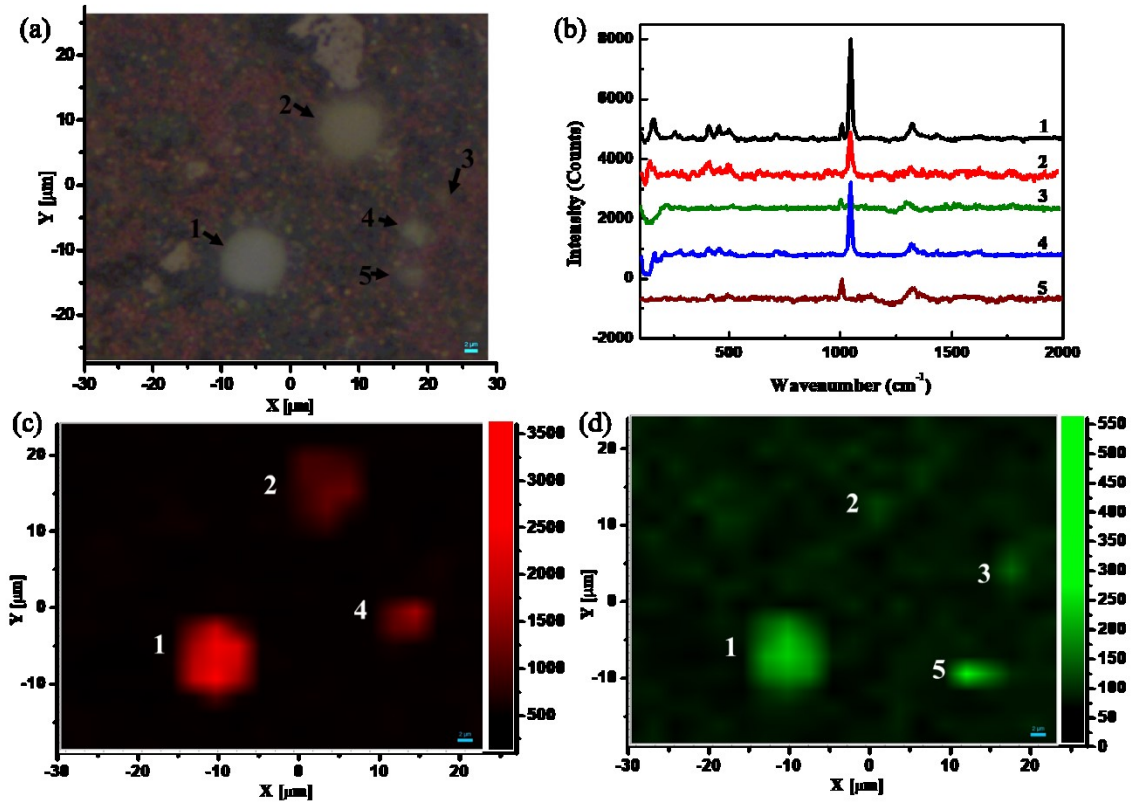

Figure 8. Identifying of ambient particles. In (a), images of the ambient particles under raman optical microscope. In (b), SERS spectra of the ambient particles. In (c) and in (d), point-by-point Raman mapping of ambient particles with different chemical composition: (c) is about nitrate and (d) is about sulfate. The mapping region is about 50 × 50 μm^2 on the Cu/Ag SSVs substrates.

CONCLUSIONS

Our results show that Cu/Ag SSVs can act as highly efficient SERS substrates. Increasing Ag content and tuning bowl shape can significantly enhance the signal intensity of the Raman spectra. The SERS EF factor of Cu/Ag SSVs was studied experimentally and theoretically. The highest intensity of $\nu(SO_4^{2-})$ around 970 cm^{-1} is 55 times higher than that detected on non-SERS substrate. This work presents great improvements on the stability and sensitivity of the SERS technique for single atmospheric aerosol particle studies. The work also demonstrates how Raman mapping

provides the distribution of chemical components in individual aerosol particles, which is challenging for other methods, such as mass spectrometry or chromatography. By revealing specific structure and enhanced detection limits, our study makes a significant contribution to individual particle analysis. Our methods can be effective tools to analyze particulate matter and could serve as probes for haze formation mechanisms, informing the general public and governance policies.

ASSOCIATED CONTENT

Supporting Information Available: Microscopy images of the obtained SERS substrate after Cu/Ag deposition with different electrochemical deposition time under Raman Optical Microscope before and after the PS spheres are etched away. Limits of detection (LOD) of $(NH_4)_2SO_4$ aerosols particles on the FTO substrate (black) and Cu/Ag SSVs substrate (red), respectively. Image of $(NH_4)_2SO_4$ aerosols particles on the Cu/Ag SSVs substrate under Raman Optical Microscope.

ACKNOWLEDGEMENTS

This material based upon work was jointly supported by National Natural Science Foundation of China (No. 21507011 and No. 21677037), Ministry of Science and Technology of the People's Republic of China (2016YFE0112200 and 2016YFC0202700), the Natural Science Foundation of Shanghai (No. 17ZR1440200), and the China Postdoctoral Science Foundation funded project (No. KLH1829019). L.O. and V.K.V. acknowledge funding and support from the Engineering and Physical Sciences Research Council (EPSRC) Centre for Doctoral Training in Condensed Matter Physics (CDT-CMP), Grant No. EP/L015544/1. V.K.V. acknowledges support from the Royal Society through the University Research Fellowships, and through grants CHG\R1\170067, PEF1\170015 and RGF\EA\180228, as well as from STFC grant ST/R005842/1.

References:

(1) Ramanathan, V.; Crutzen, P. J.; Kiehl, J. T.; Rosenfeld, D. Aerosols, Climate, and the Hydrological Cycle. Science 2001, 294, 2119.

(2) Pöschl, U. Atmospheric Aerosols: Composition, Transformation, Climate and Health Effects. Angew. Chem. Int. Edit. 2005, 44, 7520-7540.

(3) Andreae, M. O.; Rosenfeld, D. Aerosol – cloud – precipitation interactions. Part 1. The nature and sources of cloud-active aerosols. Earth-Sci. Rev. 2008, 89, 13-41.

(4) Myhre, G.; Samset, B. H.; Schulz, M.; Balkanski, Y.; Bauer, S.; Berntsen, T. K.; Bian, H.; Bellouin, N.; Chin, M.; Diehl, T.; Easter, R. C.; Feichter, J.; Ghan, S. J.; Hauglustaine, D.; Iversen, T.; Kinne, S.; Kirkevåg, A.; Lamarque, J. F.; Lin, G.; Liu, X.; Lund, M. T.; Luo, G.; Ma, X.; van Noije, T.; Penner, J. E.; Rasch, P. J.; Ruiz, A.; Seland, Ø.; Skeie, R. B.; Stier, P.; Takemura, T.; Tsigaridis, K.; Wang, P.; Wang, Z.; Xu, L.; Yu, H.; Yu, F.; Yoon, J. H.; Zhang, K.; Zhang, H.; Zhou, C. Radiative forcing of the direct aerosol effect from AeroCom Phase II simulations. Atmos. Chem. Phys. 2013, 13, 1853-1877.

(5) Bauer, M.; Pfennig, A.; Severus, E.; Whybrow, P. C.; Angst, J.; Möller, H. World Federation of Societies of Biological Psychiatry (WFSBP) Guidelines for Biological Treatment of Unipolar Depressive Disorders, Part 1: Update 2013 on the acute and continuation treatment of unipolar depressive disorders. World J. Biol. Psychia. 2013, 14, 334-385.

(6) Riemer, N.; West, M. Quantifying aerosol mixing state with entropy and diversity measures. Atmos. Chem. Phys. 2013, 13, 11423-11439.

(7) Le Quéré, C.; Moriarty, R.; Andrew, R. M.; Canadell, J. G.; Sitch, S.; Korsbakken, J. I.; Friedlingstein, P.; Peters, G. P.; Andres, R. J.; Boden, T. A.; Houghton, R. A.; House, J. I.; Keeling, R. F.; Tans, P.; Arneth, A.; Bakker, D. C. E.; Barbero, L.; Bopp, L.; Chang, J.; Chevallier, F.; Chini, L. P.; Ciais, P.; Fader, M.; Feely, R. A.; Gkritzalis, T.; Harris, I.; Hauck, J.; Ilyina, T.; Jain, A. K.; Kato, E.; Kitidis, V.; Klein Goldewijk, K.; Koven, C.; Landschützer, P.; Lauvset, S. K.; Lefèvre, N.; Lenton, A.; Lima, I. D.; Metzl, N.; Millero, F.; Munro, D. R.; Murata, A.; Nabel, J. E. M. S.; Nakaoka, S.; Nojiri, Y.; O'Brien, K.; Olsen, A.; Ono, T.; Pérez, F. F.; Pfeil, B.; Pierrot, D.; Poulter, B.;

Rehder, G.; Rödenbeck, C.; Saito, S.; Schuster, U.; Schwinger, J.; Séférian, R.; Steinhoff, T.; Stocker, B. D.; Sutton, A. J.; Takahashi, T.; Tilbrook, B.; van der Laan-Luijkx, I. T.; van der Werf, G. R.; van Heuven, S.; Vandemark, D.; Viovy, N.; Wiltshire, A.; Zaehle, S.; Zeng, N. Global Carbon Budget 2015. Earth Syst. Sci. Data 2015, 7, 349-396.

(8) Fierce, L.; Bond, T. C.; Bauer, S. E.; Mena, F.; Riemer, N. Black carbon absorption at the global scale is affected by particle-scale diversity in composition. Nat. Commun. 2016, 7, 12361.

(9) Wildt, J.; Surratt, J. D.; Seinfeld, J. H.; Prévôt, A. S. H.; Monod, A.; Mentel, T. F.; McFiggans, G.; Maenhaut, W.; Kiendler-Scharr, A.; Jenkin, M. E.; Jimenez, J. L.; Iinuma, Y.; Jang, M.; Herrmann, H.; Hoffmann, T.; Goldstein, A. H.; Hamilton, J. F.; Donahue, N. M.; George, C.; Claeys, M.; Dommen, J.; Simpson, D.; Rudich, Y.; Baltensperger, U.; Hallquist, M.; Wenger, J. C.; Szmigielski, R. The formation, properties and impact of secondary organic aerosol: current and emerging issues. Atmos. Chem. Phys. 2009, 9, 5155-5235.

(10) Virtanen, A.; Joutsensaari, J.; Koop, T.; Kannosto, J.; Yli-Pirilä, P.; Leskinen, J.; Mäkelä, J. M.; Holopainen, J. K.; Pöschl, U.; Kulmala, M.; Worsnop, D. R.; Laaksonen, A. An amorphous solid state of biogenic secondary organic aerosol particles. Nature 2010, 467, 824-827.

(11) Stefaniak, E. A.; Buczynska, A.; Novakovic, V.; Kuduk, R.; Grieken, R. V. Determination of chemical composition of individual airborne particles by SEM/EDX and micro-Raman spectrometry: A review. J. Phys.: Conf. Ser. 2009, 162, 12019.

(12) Craig, R. L.; Nandy, L.; Axson, J. L.; Dutcher, C. S.; Ault, A. P. Spectroscopic Determination of Aerosol pH from Acid – Base Equilibria in Inorganic, Organic, and Mixed Systems. J. Phys. Chem. A 2017, 121, 5690-5699.

(13) Gen, M.; Chan, C. K. Electrospray surface-enhanced Raman spectroscopy (ES-SERS) for probing surface chemical compositions of atmospherically relevant particles. Atmos. Chem. Phys. 2017, 17, 14025-14037.

(14) Avzianova, E.; Brooks, S. D. Analysis of nickel (II) in particulate matter by Raman microspectroscopy. J. Aerosol Sci. 2014, 67, 207-214.

(15) Wei, H.; Vejerano, E. P.; Leng, W.; Huang, Q.; Willner, M. R.; Marr, L. C.; Vikesland, P. J. Aerosol microdroplets exhibit a stable pH gradient. P Natl. A Sci. 2018, 115, 7272.

(16) Falgayrac, G.; Sobanska, S.; Brémard, C. Raman diagnostic of the reactivity between ZnSO4 and CaCO3 particles in humid air relevant to heterogeneous zinc chemistry in atmosphere. Atmos. Environ. 2014, 85, 83-91.

(17) Andreae, M. O.; Gelencsér, A. Black carbon or brown carbon? The nature of light-absorbing carbonaceous aerosols. Atmos. Chem. Phys. 2006, 6, 3131-3148.

(18) Schweiger, G. Raman scattering on single aerosol particles and on flowing aerosols: a review. J. Aerosol Sci. 1990, 21, 483-509.

(19) Zheng, L.; Kulkarni, P.; Birch, M. E.; Ashley, K.; Wei, S. Analysis of Crystalline Silica Aerosol Using Portable Raman Spectrometry: Feasibility of Near Real-time Measurement. Anal. Chem. 2018, 90, 6229-6239.

(20) Kneipp, K.; Kneipp, H.; Itzkan, I.; Dasari, R. R.; Feld, M. S. Ultrasensitive Chemical Analysis by Raman Spectroscopy. Chem. Rev. 1999, 99, 2957-2976.

(21) Campion, A.; Kambhampati, P. Surface-enhanced Raman scattering. Chem. Soc. Rev. 1998, 27, 241-250.

(22) Halvorson, R. A.; Vikesland, P. J. Surface-Enhanced Raman Spectroscopy (SERS) for Environmental Analyses. Environ. Sci. Technol. 2010, 44, 7749-7755.

(23) Tirella, P. N.; Craig, R. L.; Tubbs, D. B.; Olson, N. E.; Lei, Z.; Ault, A. P. Extending surface enhanced Raman spectroscopy (SERS) of atmospheric aerosol particles to the accumulation mode (150 – 800 nm). Environ. Sci.: Processes Impacts 2018, 20, 1570-1580.

(24) Ofner, J.; Deckert-Gaudig, T.; Kamilli, K. A.; Held, A.; Lohninger, H.; Deckert, V.; Lendl, B. Tip-Enhanced Raman Spectroscopy of Atmospherically Relevant Aerosol Nanoparticles. Anal. Chem. 2016, 88, 9766-9772.

(25) Gen, M.; Kunihisa, R.; Matsuki, A.; Chan, C. K. Electrospray surface-enhanced Raman spectroscopy (ES-SERS) for studying organic coatings of atmospheric aerosol particles. Aerosol Sci. Tech. 2019, 53, 1-11.

(26) Sivaprakasam, V.; Hart, M. B.; Eversole, J. D. Surface Enhanced Raman Spectroscopy of Individual Suspended Aerosol Particles. J. Phys. Chem. C 2017, 121, 22326-22334.

(27) Ayora, M. J.; Ballesteros, L.; Pérez, R.; Rupérez, A.; Laserna, J. J. Detection of atmospheric contaminants in aerosols by surface-enhanced Raman spectrometry. Anal. Chim. Acta 1997, 355, 15-21.

(28) Sengupta, A.; Laucks, M. L.; Dildine, N.; Drapala, E.; Davis, E. J. Bioaerosol characterization by surface-enhanced Raman spectroscopy (SERS). J. Aerosol Sci. 2005, 36, 651-664.

(29) Schwarzmeier, K.; Knauer, M.; Ivleva, N. P.; Niessner, R.; Haisch, C. Bioaerosol analysis based on a label-free microarray readout method using surface-enhanced Raman scattering. Anal. Bioanal. Chem. 2013, 405, 5387-5392.

(30) Craig, R. L.; Bondy, A. L.; Ault, A. P. Surface Enhanced Raman Spectroscopy Enables Observations of Previously Undetectable Secondary Organic Aerosol Components at the Individual Particle Level. Anal. Chem. 2015, 87, 7510-7514.

(31) Fu, Y.; Kuppe, C.; Valev, V. K.; Fu, H.; Zhang, L.; Chen, J. Surface-Enhanced Raman Spectroscopy: A Facile and Rapid Method for the Chemical Component Study of Individual Atmospheric Aerosol. Environ. Sci. Technol. 2017, 51, 6260-6267.

(32) Sun, Z.; Duan, F.; He, K.; Du, J.; Zhu, L. Sulfate – nitrate – ammonium as double salts in PM2.5: Direct observations and implications for haze events. Sci. Total Environ. 2019, 647, 204-209.

(33) Cui, L.; Mahajan, S.; Cole, R. M.; Soares, B.; Bartlett, P. N.; Baumberg, J. J.; Hayward, I. P.; Ren, B.; Russell, A. E.; Tian, Z. Q. UV SERS at well ordered Pd sphere segment void (SSV) nanostructures. Phys. Chem. Chem. Phys. 2009, 11, 1023-1026.

(34) Johnson, R. P.; Mahajan, S.; Abdelsalam, M. E.; Cole, R. M.; Baumberg, J. J.; Russell, A. E.; Bartlett, P. N. SERS from two-tier sphere segment void substrates. Phys. Chem. Chem. Phys. 2011, 13, 16661-16665.

(35) Mahajan, S.; Cole, R. M.; Soares, B. F.; Pelfrey, S. H.; Russell, A. E.; Baumberg, J. J.; Bartlett, P. N. Relating SERS Intensity to Specific Plasmon Modes on Sphere Segment Void Surfaces. J. Phys. Chem. C 2009, 113, 9284-9289.

(36) Lumerical Nanophotonic FDTD Simulation Software - Lumerical FDTD. https://www.lumerical.com/products/fdtd/, 2019.
(37) Taflove A; Hagness S C Computational Electrodynamics: The Finite-Difference Time-Domain Method. 2010, Artech House: Boston.
(38) Montgomery, J. M.; Lee, T.; Gray, S. K. Theory and modeling of light interactions with metallic nanostructures. Journal of Physics: Condensed Matter 2008, 20, 323201.
(39) Kane, Y. Numerical solution of initial boundary value problems involving maxwell's equations in isotropic media. IEEE T. Antenn. Propag. 1966, 14, 302-307.
(40) J., B. Perfectly matched layer for the FDTD solution of wave-structure interaction problems. IEEE T. Antenn. Propag. 1996, 44, 110-117.
(41) Orendorff, C. J.; Murphy, C. J. Quantitation of Metal Content in the Silver-Assisted Growth of Gold Nanorods. J. Phys. Chem. B 2006, 110, 3990-3994.
(42) Jiang, R.; Chen, H.; Shao, L.; Li, Q.; Wang, J. Unraveling the Evolution and Nature of the Plasmons in (Au Core) − (Ag Shell) Nanorods. Adv. Mater. 2012, 24, P200-P207.
(43) Erol, M.; Han, Y.; Stanley, S. K.; Stafford, C. M.; Du, H.; Sukhishvili, S. SERS Not To Be Taken for Granted in the Presence of Oxygen. J. Am. Chem. Soc. 2009, 131, 7480-7481.
(44) Pietrobon, B.; McEachran, M.; Kitaev, V. Synthesis of Size-Controlled Faceted Pentagonal Silver Nanorods with Tunable Plasmonic Properties and Self-Assembly of These Nanorods. ACS Nano 2009, 3, 21-26.
(45) Zhou, Y.; Rees, N. V.; Compton, R. G. The Electrochemical Detection and Characterization of Silver Nanoparticles in Aqueous Solution. Angew. Chem. Int. Edit. 2011, 50, 4219-4221.
(46) Lu, P.; Chandross, M.; Boyle, T. J.; Clark, B. G.; Vianco, P. Equilibrium Cu-Ag nanoalloy structure formation revealed by in situ scanning transmission electron microscopy heating experiments. APL Materials 2014, 2, 22107.
(47) Cole, R. M.; Baumberg, J. J.; Garcia De Abajo, F. J.; Mahajan, S.; Abdelsalam, M.; Bartlett, P. N. Understanding Plasmons in Nanoscale Voids. Nano Lett. 2007, 7, 2094-2100.

(48) Johnson, R. P.; Mahajan, S.; Abdelsalam, M. E.; Cole, R. M.; Baumberg, J. J.; Russell, A. E.; Bartlett, P. N. SERS from Two-tier Sphere Segment Void Substrates. Phys. Chem. Chem. Phys. 2011, 13, 16661-16665.

(49) Cintra, S.; Abdelsalam, M. E.; Bartlett, P. N.; Baumberg, J. J.; Kelf, T. A.; Sugawara, Y.; Russell, A. E. Sculpted Substrates for SERS. Faraday Discuss. 2006, 132, 191-199.

(50) Baumberg, J. J.; Kelf, T. A.; Sugawara, Y.; Cintra, S.; Abdelsalam, M. E.; Bartlett, P. N.; Russell, A. E. Angle-Resolved Surface-Enhanced Raman Scattering on Metallic Nanostructured Plasmonic Crystals. Nano Lett. 2005, 5, 2262-2267.

(51) Ault, A. P.; Moffet, R. C.; Baltrusaitis, J.; Collins, D. B.; Ruppel, M. J.; Cuadra-Rodriguez, L. A.; Zhao, D.; Guasco, T. L.; Ebben, C. J.; Geiger, F. M.; Bertram, T. H.; Prather, K. A.; Grassian, V. H. Size-Dependent Changes in Sea Spray Aerosol Composition and Properties with Different Seawater Conditions. Environ. Sci. Technol. 2013, 47, 5603-5612.

(52) Vargas Jentzsch, P.; Kampe, B.; Ciobotă, V.; Rösch, P.; Popp, J. Inorganic salts in atmospheric particulate matter: Raman spectroscopy as an analytical tool. Spectrochim. Acta, Part A 2013, 115, 697-708.

(53) Zhou, Q.; Pang, S.; Wang, Y.; Ma, J.; Zhang, Y. Confocal Raman Studies of the Evolution of the Physical State of Mixed Phthalic Acid/Ammonium Sulfate Aerosol Droplets and the Effect of Substrates. J. Phys. Chem. B 2014, 118, 6198-6205.

(54) Hashimoto, Y.; Seniutinas, G.; Balčytis, A.; Juodkazis, S.; Nishijima, Y. Au-Ag-Cu nano-alloys: tailoring of permittivity. Sci. Rep.-UK 2016, 6, 25010.

(55) Spillane, S. M.; Kippenberg, T. J.; Vahala, K. J. Ultralow-threshold Raman laser using a spherical dielectric microcavity. Nature 2002, 415, 621-623.

(56) Ault, A. P.; Guasco, T. L.; Baltrusaitis, J.; Ryder, O. S.; Trueblood, J. V.; Collins, D. B.; Ruppel, M. J.; Cuadra-Rodriguez, L. A.; Prather, K. A.; Grassian, V. H. Heterogeneous Reactivity of Nitric Acid with Nascent Sea Spray Aerosol: Large Differences Observed between and within Individual Particles. J. Phys. Chem. Letters 2014, 5, 2493-2500.

For Table of Contents Only